Heliyon 10 (2024) e29676

Contents lists available at ScienceDirect

Heliyon

journal homepage: www.cell.com/heliyon

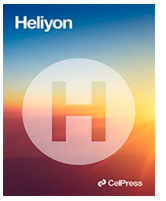

Research article

Mixed cations tin-germanium perovskite: A promising approach for enhanced solar cell applications

Mohd Saiful Adli Azizman [a,b], Ayu Wazira Azhari [a,b,*], Naimah Ibrahim [a,b], Dewi Suriyani Che Halin [c,d], Suhaila Sepeai [e], Norasikin Ahmad Ludin [e], Mohammad Nuzaihan Md Nor [f], Li Ngee Ho [b,c]

[a] *Faculty of Civil Engineering and Technology, Universiti Malaysia Perlis, 02600, Jalan Kangar-Arau, Perlis, Malaysia*
[b] *Center of Excellence for Water Research and Environmental Sustainability Growth (WAREG), Universiti Malaysia Perlis, 02600, Jalan Kangar-Arau, Perlis, Malaysia*
[c] *Faculty of Chemical Engineering and Technology, Universiti Malaysia Perlis, 02600, Jalan Kangar-Arau, Perlis, Malaysia*
[d] *Center of Excellence for Geopolymer & Green Technology (CEGeoGTech), Universiti Malaysia Perlis, (UniMAP), 02600, Jalan Kangar-Arau, Perlis, Malaysia*
[e] *Solar Energy Research Institute (SERI), Universiti Kebangsaan Malaysia (UKM), Bangi, Selangor, Malaysia*
[f] *Institute of Nano Electronic Engineering (INEE), Universiti Malaysia Perlis (UniMAP), Kangar, Perlis, Malaysia*

A R T I C L E I N F O

Keywords:
Compositional engineering
Perovskite solar cells
Mixed cations
SnGe
SCAPS 1-D

A B S T R A C T

Significant progress has been made over the years to improve the stability and efficiency of rapidly evolving tin-based perovskite solar cells (PSCs). One powerful approach to enhance the performance of these PSCs is through compositional engineering techniques, specifically by incorporating a mixed cation system at the A-site and B-site structure of the tin perovskite. These approaches will pave the way for unlocking the full potential of tin-based PSCs. Therefore, in this study, a theoretical investigation of mixed A-cations (FA, MA, EA, Cs) with a tin-germanium-based PSC was presented. The crystal structure distortion and optoelectronic properties were estimated. SCAPS 1-D simulations were employed to predict the photovoltaic performance of the optimized tin-germanium material using different electron transport layers (ETLs), hole transport layers (HTLs), active layer thicknesses, and cell temperatures. Our findings reveal that $EA_{0.5}Cs_{0.5}Sn_{0.5}Ge_{0.5}I_3$ has a nearly cubic structure (t = 0.99) and a theoretical bandgap within the maximum Shockley-Queisser limit (1.34 eV). The overall cell performance is also improved by optimizing the perovskite layer thickness to 1200 nm, and it exhibits remarkable stability as the temperature increases. The short-circuit current density (J_{sc}) remains consistent around 33.7 mA/cm^2, and the open-circuit voltage (V_{oc}) is well-maintained above 1 V by utilizing FTO as the conductive layer, ZnO as the ETL, Cu_2O as the HTL, and Au as the metal back contact. This configuration also achieves a high fill factor ranging from 87 % to 88 %, with the highest power conversion efficiency (PCE) of 31.49 % at 293 K. This research contributes to the advancement of tin-germanium perovskite materials for a wide range of optoelectronic applications.

* Corresponding author. Faculty of Civil Engineering and Technology, Universiti Malaysia Perlis, 02600, Jalan Kangar-Arau, Perlis, Malaysia.
E-mail address: ayuwazira@unimap.edu.my (A.W. Azhari).

https://doi.org/10.1016/j.heliyon.2024.e29676
Received 10 September 2023; Received in revised form 25 March 2024; Accepted 12 April 2024
Available online 16 April 2024

1. Introduction

Compositional engineering (CE) is an effective approach for improving the performance of various applications, such as light-emitting diodes, perovskite solar cells, and photodetectors. It also has the potential to create new opportunities for future optoelectronic devices by increasing their effectiveness, stability, and ecological sustainability [1–4]. In the case of perovskite solar cells (PSCs), CE is used to systematically modify and optimize the composition and/or material of ABX_3, where A and B are cations, and X is an anion in the crystal structure of perovskite materials. By changing the A, B, and X components of perovskite materials, CE can provide desired features such as improved stability, better light absorption, and higher charge carrier mobility [5]. The A-site cation can be modified to alter the lattice properties and crystal structure of perovskites. This allows for control over the bandgap and stability of perovskite materials by using different A-site cations [6]. On the other hand, the B-site cation influences the electrical and optical characteristics of perovskites. By changing the metal ions at the B-site, it is possible to customize defect formation, carrier transport, and bandgap in perovskite materials, leading to greater stability [7].

In recent years, there has been a significant increase of interest in compositional engineering for tin-based perovskite materials, specifically hybrid organic-inorganic tin (Sn) halide perovskites. According to Scopus statistics, there have been 2751 research articles on Sn-based perovskite in just 5 years (2018–2022) [8]. The focus of these studies are on replacing lead (Pb) with tin (Sn) in perovskite materials to overcome the drawbacks associated with Pb-based perovskites, particularly concerns about toxicity [9].

One of the main drawbacks of Sn-based perovskites compared to their Pb-based counterparts is their intrinsic volatility. To address this, researchers have been exploring various approaches to increase their stability. Compositional engineering has proven to be highly significant in this regard, as it has improved the stability of Sn-based perovskites by incorporating different A-site cations into the Sn structure [10]. This technique also allows for control over the bandgap of Sn-based perovskite materials, making them suitable for a range of optoelectronic devices with specific application requirements [11].

Typically, organic A-cations such as formamidinium (FA), methylammonium (MA), and caesium (Cs) are used in PSCs. However, studies have shown that incorporating ethylammonium (EA) into the perovskite structure can result in improved power conversion efficiencies and long-term stability [12]. EA has some unique properties that make it an interesting substitute. For example, its larger size (2.74 Å) compared to other cations can help increase the structural stability of the perovskite material. Additionally, the presence of EA can slow down ion migration, which can improve the stability of the perovskite film. The larger size of the EA cation can also help suppress the formation of defects within the crystal lattice, leading to longer carrier lifetimes and higher charge carrier mobilities. These factors contribute to enhanced overall device performance by reducing recombination losses and improving charge extraction [13,14].

In addition to Pb and Sn, germanium (Ge), which is a lighter member of group IV, can also be used to make perovskite [15]. However, similar to Sn^{2+} materials, Ge-based perovskites have the same characteristics as Sn-based PSCs, where Ge^{2+} is also prone to oxidation into stable Ge^{4+}. The smaller radius of Ge (~73 p.m.) compared to Pb (~119 p.m.) and Sn (~115 p.m.) results in instability in the ABX_3 structure [16]. Perovskites with mono-cations (A; FA, MA, Cs) and germanium triiodide ($AGeI_3$) have shown to have a wider bandgap, ranging from 1.6 eV to 2.2 eV, respectively. However, this wide bandgap in Ge-based PSCs ($FAGeI_3$>$MAGeI_3$>$CsGeI_3$) results in poor performance, with power conversion efficiency (PCE) of less than 0.20 % [17]. On the contrary, only ethylammonium germanium triiodide ($EAGeI_3$) shows a theoretically calculated bandgap around 1.3 eV [18]. Additionally, the wide bandgap in Ge-based PSCs is too large to successfully absorb light, making Ge-based perovskites unsuitable to be used alone. Instead, they are often alloyed with other metals, such as Sn-based perovskites, or used as tandem perovskites via charge extraction, due to the challenges in performance [19,20].

Alloying Ge with Sn-based materials or vice versa through compositional engineering can enhance device performance and reduce defects [21]. When Ge is mixed with Sn-based materials, the Ge atoms can replace Sn atoms in the crystal structure. This substitution helps prevent the formation of vacancies that can occur when Sn atoms are absent. The addition of Ge fills these vacancies, stabilizing the crystal structure and reducing defects. Ge can also act as a substitute ion, specifically Ge^{2+}, which helps maintain the charge balance in the crystal lattice and reduces the occurrence of charged defects [22]. Charged defects can negatively affect the electrical and optical properties of the material [23]. By alloying Ge with Sn-based materials, the number of defects is reduced, and the crystal lattice is stabilized, leading to improved device performance. This, in turn, improves the optoelectronic characteristics and stability of Sn-based perovskite [22]. Additionally, compositional engineering can be used to introduce passivating agents or surface modifications that decrease trap states and prolong the lifetimes of charge carriers [24]. These approaches have been successful in enhancing the performance and stability of Sn-based perovskite devices [25].

Interestingly, combining mixed A cations with alloyed B cations in perovskites allows for even greater control over the material properties. These combinations can lead to improved stability, enhanced light absorption, and optimized charge transport properties [26]. One notable example is the synthesis of mixed-cation perovskites by incorporating mixed A-cations (FAMA) into an alloyed Sn–Ge perovskite structure. The evaluation of the perovskite materials' electrical and optical properties using ultraviolet–visible spectrophotometry and photoacoustic spectroscopy revealed that the materials' bandgap values ranged from 1.40 to 1.53 eV, supporting the idea that mixed A cations with alloyed B cations can be used for solar cell applications. The device's performance improved from 3.31 % to 4.48 % due to reduced defects and lower trap density in the perovskite material [27]. The use of mixed A cations with alloyed B cations has demonstrated promising results in improving device performance, stability, and efficiency [28,29].

To date, a total of 42 articles on SnGe thin film have been published until 2022. Out of these, 24 % of researchers have successfully synthesized SnGe perovskite, while 19 papers focused on theoretical calculations. However, only 3 simulation studies have been conducted so far. The majority of studies on mixed A-cations (19 % of them) have used a combination of FA, MA, Cs, and occasionally other materials such as ethylenediamine, phenethylamine, rubidium, potassium, and butylammonium in their theoretical,

experimental, and simulation approaches [30].

The choice of specific mixed A and B cation combinations depends on the desired properties and performance requirements for the intended applications. Continuous exploration of new combinations and optimization of the ratios of these cations through compositional engineering are crucial to achieving the desired balance between stability and efficiency in Sn-based perovskites. While mixed cations offer advantages such as improved stability, careful optimization of the cation combinations and ratios is necessary to avoid detrimental effects on the material properties. The stability and performance of mixed cation Sn-based perovskites are still actively researches and ongoing efforts aim to further understand and optimize these systems for practical applications. However, the specific combination of mixed A-site cations with alloyed B-site cations in perovskite has not been extensively explored. Therefore, we present the first theoretical and numerical simulation insight into mixed A-site cations with alloyed Sn–Ge PSC, through a compositional engineering technique.

2. Materials and methods

2.1. Crystal structure

This study describes the estimation of the crystal structure (Fig. 1) of hybrid perovskite ($A_xA'_{1-x}B_yB'_{1-y}X_3$) with mixed A cations (formamidinium; FA, methylammonium; MA, ethylammonium; EA, caesium; Cs), mixed B cations (tin; Sn, germanium; Ge), and X anion (iodide, I). The crystal structure is characterized using the octahedral factor and tolerance factor. The octahedral factor (Eq. (1)) and the tolerance factor (Eq. (2)) are terms used to describe the geometry of a crystal structure, particularly in relation to perovskite-like structures.

The octahedral factor (μ) measures the distortion from a perfect octahedral coordination geometry in B cations with different values of y (0, 0.25, 0.5, 0.75, and 1). The tolerance factor (t) describes the distortion in overall perovskite structures with a value of x = 0.5. The elemental atomic radii ($r_{AA'}$ (Eq. (3)), $r_{BB'}$ (Eq. (4)) and r_X) are given in angstrom (Å) and can be found in Table 1 [31]. The main A and B cations are denoted as A and B, while the doped cations are denoted as A′ and B′, respectively. A μ value greater than 0.41 indicates a stable structure [32], and a tolerance factor (t) between 0.9 and 1 indicates that the structure is more likely to be cubic and can form a perovskite structure [33].

$$\mu = \frac{r_{BB'}}{r_X} \tag{1}$$

$$t = \frac{r_{AA'} + r_X}{\sqrt{2}(r_{BB'} + r_X)} \tag{2}$$

$$r_{AA'} = (x)r_A + (1-x)r_{A'} \tag{3}$$

$$r_{BB'} = (y)r_B + (1-y)r_{B'} \tag{4}$$

2.2. Optoelectronic properties

Predicting the optoelectronic properties, particularly the bandgap, of mixed cation perovskite materials can be challenging due to their complex nature. However, an empirical model is often used as an initial overview of these novel materials. In this study, a simple linear interpolation model is adapted, assuming a linear relationship between the lattice constant and the bandgap of a mixed compound based on the compositions of its constituents. This model is compared with the Shockley-Queisser (SQ) limit for Sn-based perovskite solar cells (PSCs), which falls between 1.2 and 1.4 eV [34]. The bandgap of a mono A-cation with mixed B-cations ($ASnGeI_3$) is derived from pure materials (Table 2) using Eq. (5), while Eq. (6) is used for mixed cations ($AA'SnGeI_3$) and derived from the bandgap of mono A-cations into SnGe with x, y = 0.5. The bandgap is denoted as E_g (eV), with mono and mixed A-site cations

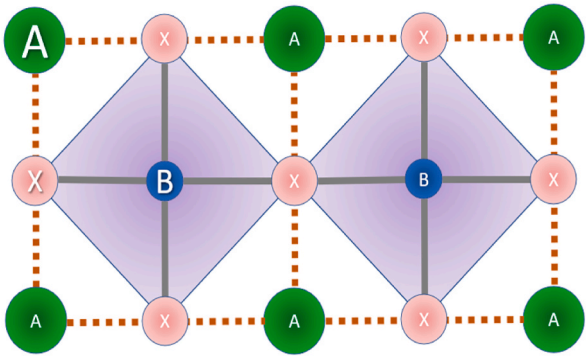

Fig. 1. Crystal structure of perovskite (ABX_3).

Table 1
Atomic radii of proposed materials [31].

Element	Atomic radii (Å)
Sn^{2+}	1.15
Ge^{2+}	0.73
FA^{+}	2.53
MA^{+}	2.17
EA^{+}	2.74
Cs^{+}	1.67
I^{-}	2.20

Table 2
Pure Sn and Ge bandgap in ABX_3 [18,35–38].

Sample	Band Gap (eV)
$FASnI_3$	1.4
$FAGeI_3$	2.2
$MASnI_3$	1.3
$MAGeI_3$	1.9
$EASnI_3$	1.17
$EAGeI_3$	1.3
$CsSnI_3$	1.3
$CsGeI_3$	1.6

represented by A, A' = FA, MA, EA, Cs, and mixed B-site cations represented by BB' = SnGe, respectively [35–38].

$$E_g\left(\mathrm{AB}_y B'_{1-y}\right) = yE_g(AB) + (1-\mathrm{y})E_g(AB') \tag{5}$$

$$E_g\left(A_x A'_{1-x} BB'\right) = xE_g(ABB') + (1-x)E_g(A'BB') \tag{6}$$

2.3. Numerical simulation study

The simulation study [39] was conducted to verify the simulation parameters and revalidate them under the illumination of AM1.5G spectrum, 1000 w/m^2, and 300 K (K). This was done using a one-dimensional solar cell capacitance simulator (SCAPS 1-D) [40]. The active layer material used was caesium tin germanium triiodide ($CsSnGeI_3$), and the transparent conductive layer (TCO) was made of fluorine tin oxide (FTO). Additionally, titanium dioxide (TiO_2), 2,2′,7,7′-tetrakis(N,N-di-*p*-methoxyphenylamine)-9,9′-spirobifluorene (Spiro-OMeTAD), and gold (Au) were used as the electron transport layer (ETL), hole transport layer (HTL), and metal back contact, respectively. The layer thickness in the validation model was modified, and it served as the base model for the optimization study, as shown in Fig. 2(a and b).

The study aimed to optimize the performance of mixed cation SnGe perovskite solar cells (PSCs) by using different electron transport layers (ETL) such as zinc oxide (ZnO), tin (iv) oxide (SnO_2), tungsten (iv) oxide (WO_3), and indium gallium zinc oxide (IGZO), as well as different hole transport layers (HTL) including copper oxide (Cu_2O), poly(3,4-ethylenedioxythiophene): polystyrene sulfonate (PEDOT:PSS), poly(3-hexylthiophene-2,5-diyl) (P3HT), and graphene oxide (GO). The effects of active layer thickness (ALT) ranging from 300 to 1500 nm and cells operating temperature (T) ranging from 293 to 313 K (K) were also investigated.

Table 3 to Table 7 present the initial material parameters considered in the simulation which are the front and back metal contacts [41] (Table 3), defects [39] (Table 4), electrical properties (Table 5) and the ETL (Table 6) and HTL (Table 7) properties. These parameters were obtained from published experimental, theoretical, and simulation works [42–45]. The parameters include layer

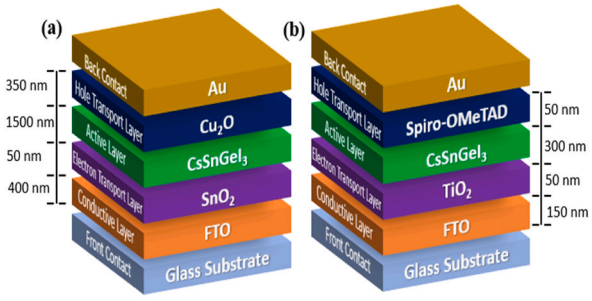

Fig. 2. Cell architecture. (a) Validation model, (b) base model.

Table 3
Properties of front and back metal contact [41].

Parameter	Front contact	Back contact
		Au
Work function (eV)	4.4	5.1
Electrons surface recombination velocity (cm/s)	1×10^5	1×10^7
Holes surface recombination velocity (cm/s)	1×10^7	1×10^5

Table 4
Defect properties of reference and base model [39].

Parameter	ETL/AL	AL/HTL	ETL	AL	HTL
Defect type	Neutral				
σ_n	1×10^{-15}				
σ_p	1×10^{-15}				
N_t	1×10^{12}		1×10^{15}		
Energetic distribution	Single	Single	Single	Gaussian	Single
E_t	0.6 eV above highest E_v				

Table 5
Electrical properties of base and optimization model [39].

Parameter	TCO	ETL	AL		HTL
	FTO	SnO_2	$CsSnGeI_3$	AA'$SnGeI_3$	Cu_2O
th	0.15	0.05	0.3	0.3–1.5	0.05
E_g	3.5	3.6	1.5	This study	2.17
χ	4.4	3.9	3.9		3.2
ε_r	9	8	28		7.11
N_c	2.2×10^{18}	3.16×10^{18}	3.1×10^{18}		2×10^{17}
N_v	1.8×10^{19}	2.5×10^{19}	3.1×10^{19}		1.1×10^{19}
μn	20	15	974		20
μh	10	0.1	213		80
N_d	1×10^{18}	1×10^{17}	0		1×10^7
N_a	0	0	1×10^{19}		1×10^{18}

Table 6
Properties of different ETL [41–44].

Parameter	ETL			
	TiO_2	ZnO	WO_3	IGZO
th	0.05			
E_g	3.2	3.3	3	3.05
χ	4	4	4.1	4.16
ε_r	10	9	5.76	10
N_c	5×10^{19}	3.7×10^{19}	1.96×10^{19}	5×10^{18}
N_v	5×10^{19}	1.8×10^{19}	1.96×10^{19}	5×10^{18}
μn	6×10^{-3}	100	10	15
μh	6×10^{-3}	25	10	0.1
N_d	1×10^{18}	1×10^{18}	3.68×10^{19}	1.8×10^{18}
N_a	0			

thickness (*th*) in micrometres (μm), bandgap (E_g) in electron volts (eV), electron affinity (χ) in eV, relative dielectric permittivity (ε_r) in dimensionless units, conductive and valence band density of states (N_c and N_v) in cm^{-3}, electron and hole mobility (μn and μh) in cm^2/Vs, donor and acceptor concentration (N_d and N_a) in cm^{-3}, defect density (N_t) in cm^{-3}, electron and hole capture cross section (σ_n and σ_p) in cm^{-2}, and energy with respect to reference (E_t) in eV.

The thermal velocity of electrons and holes for this study was set at 1×10^7 cm/s while the absorption constant used for all materials is 1×10^5 cm^{-1}. The absorption coefficient (α) is given by Eq. (7), where A is absorption constant, E is photon energy and λ is wavelength. Similar absorption interpolation was also used in other studies incorporating mixed cations SnGe-based PSCs [46–48].

$$\alpha(\lambda) = (A)\left(E - E_g\right)^{0.5} \tag{7}$$

Defects in the bulk layers and between layers (ETL/AL and AL/HTL) were also included in the cell architecture to ensure reliable

Table 7
Properties of different HTL [42,45].

Parameter	HTL			
	PEDOT:PSS	Spiro-OMeTAD	P3HT	GO
th	0.05			
E_g	1.6	3	1.7	2.48
χ	3.4	2.2	3.5	2.3
ε_r	3	3	3	10
N_c	2.2×10^{18}	2.2×10^{18}	2×10^{21}	2.5×10^{18}
N_v	1.8×10^{19}	1.8×10^{18}	2×10^{21}	2.2×10^{17}
μn	4.5×10^{-2}	2.1×10^{-3}	1.8×10^{-3}	26
μh	4.5×10^{-2}	2.16×10^{-3}	1.86×10^{-2}	123
N_d	0			
N_a	1×10^{18}	1×10^{18}	1×10^{18}	2×10^{18}

conditions were observed. The best performance among the optimized materials was highlighted and compared with $CsSnGeI_3$, which served as the control variable for this study.

3. Results and discussions

3.1. Structure characteristic

To maintain charge neutrality, the cations in the A-site occupy the voids in the 3D network formed by the corner-sharing BX_6 octahedra in the ABX_3 perovskite structure. The stability of the BX_6 octahedra is determined by the octahedral factor (μ), which takes into account the ionic size limitations imposed by the X_6 octahedron. The inclusion of the B-site cation is restricted based on these limitations [49]. An estimation of distortion in the proposed mixed B cation ($Sn_yGe_{1-y}I_3$; y = 0, 0.25, 0.5, 0.75, 1) shows that a mixed composition of Sn and Ge at equivalent concentrations and above (<50 %) can theoretically produce a stable structure with $\mu \geq 0.41$, as shown in Fig. 3. The ratio of mixed $Sn_{0.5}Ge_{0.5}$ ($r_{BB'} = 0.94$ Å) compounds with iodide ($r_X = 2.2$ Å) produces stable structures ($\mu = 0.427$) due to the phenomenon known as substitutional solid solution. This proves that Sn atoms can be substituted with Ge atoms in a crystal lattice, as described by Hume-Rotary rules [50].

The stable structure of $Sn_{0.5}Ge_{0.5}I_3$ is due to the similar chemical properties of Sn and Ge, as they both belong to Group 14 in the periodic table. They have similar configurations of four valence electrons in their highest-energy orbitals (Ge; $4s^24p^2$ and Sn; $5s^25p^2$) and exhibit similar bonding behaviours, such as covalent and metallic bonding. This similarity allows them to substitute for each other in crystal structures without causing significant disruptions. Additionally, they have comparable atomic radii, which allows for easy substitution without creating strain or distortion in the lattice. Furthermore, both Sn and Ge commonly exhibit a $^{+4}$ oxidation state, indicating their ability to maintain the same valence state. This facilitates their substitution in crystal structures without introducing significant charge imbalances [51]. By incorporating Ge into a Sn-based crystal lattice, or vice versa, a solid solution can form, maintaining the overall stability of the structure. This substitution can provide unique properties and allow for the tuning of the material's physical, chemical, or electronic characteristics, making it valuable for optoelectronics applications [27]. Therefore, $Sn_{0.5}Ge_{0.5}I_3$ is selected as the mixed B-cations for further investigation.

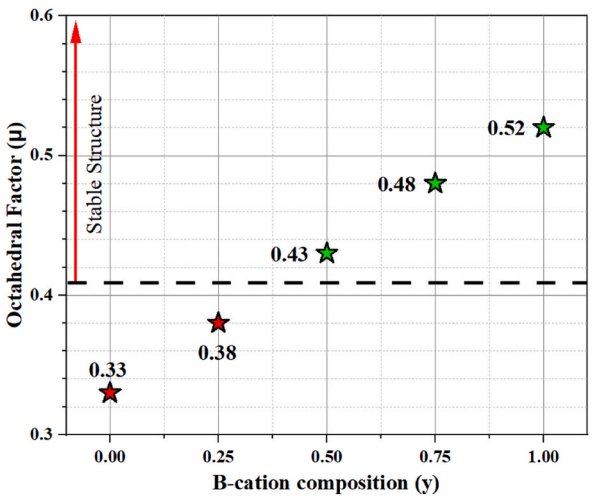

Fig. 3. Octahedral factor of SnGe.

In order for the A, B, and X ions to form structures resembling perovskites, their ionic radii must satisfy the conditions for the Goldschmidt tolerance factor (*t*). The formability and stability range for ABX_3 perovskite structures are empirically determined based on the ionic size limits for the relevant cations and anions. This suggests the existence of a cubic-crystalline structure in ABX_3. Fig. 4 shows an $A_xA_{1-x}Sn_{0.5}Ge_{0.5}I_3$ structure with A cation materials consisting of a combination of FAMA, FAEA, FACs, MAEA, MACs, and EACs, with x at 0.5. Calculated results show that the cubic perovskite structure (t = 0.9 to 1) can be formed with MA/FA/EA doped with $CsSnGeI_3$ (t = 0.93, 0.97, 0.99) respectively. Meanwhile, other compositions (FAMA, MAEA, and FAEA) have a hexagonal structure with t values greater than 1.

Several factors contribute to the nearly cubic structure of $EACsSnGeI_3$ (0.99) compared to $FACsSnGeI_3$ (0.97) and $MACsSnGeI_3$ (0.93). One factor is that the atomic radii of the EACs, Sn, and Ge cations, as well as the I anion, are relatively well-matched. This balanced size relationship between the A-site and B-site cations, along with the X-anions, leads to minimal distortion from the ideal cubic perovskite structure [52]. Additionally, the presence of strong ionic bonds between the A-site and B-site cations and the X-anions is crucial for maintaining structural stability and minimizing distortion. The balanced ionic interactions help keep the atoms close together, allowing the compound to approach a cubic arrangement [53]. Furthermore, the specific arrangement and bonding preferences within the crystal lattice can contribute to the high tolerance factor [54].

The arrangement of these ions and the resulting crystal structure may facilitate a nearly cubic geometry with minimal distortion. However, other factors such as temperature, pressure, and chemical composition can also influence the tolerance factor and the resulting crystal structure [55]. Further experimental validation and advances in computational modelling can provide additional information on the specific factors contributing to the tolerance factor of 0.99 in $EACsSnGeI_3$.

3.2. Optoelectronic properties

Vegard's Law can be used to estimate the relationship between the lattice parameter and the composition of a solid solution. It can also be used to infer certain optoelectronic properties, especially in the case of alloyed perovskite materials [56]. The bandgap energy of a material determines the range of wavelengths of light it can absorb or emit. In the case of new alloyed perovskites and limited experimental data, Vegard's Law can provide an initial estimate of the bandgap energy based on the composition of the proposed materials [57]. By considering the calculated tolerance factor in doped $CsSnGeI_3$ into FA, MA, and EA, the structure of perovskite can be resembled. The bandgap predictions of $EACsSnGeI_3$, $FACsSnGeI_3$, and $MACsSnGeI_3$ are tabulated in Table 8, which describes the theoretical estimation of mixed cations SnGe from pure single Sn and Ge mixtures.

The material $EACsSnGeI_3$ has a bandgap of 1.34 eV, which falls within the optimal range suggested by the Shockley-Queisser (SQ) limit for Sn-based perovskite materials. This indicates that the material has good light absorption properties and has the potential to efficiently convert solar energy. The SQ limit is a theoretical upper limit for the efficiency of a solar cell, and it states that the maximum efficiency is achieved when the bandgap of the material matches the energy of photons in the solar spectrum [58]. For Sn-based perovskites, a bandgap of around 1.2–1.4 eV is considered optimal because it allows for efficient absorption of visible light and a significant portion of the solar spectrum [59].

The fact that the theoretical bandgap of $EACsSnGeI_3$ falls within the optimal range suggests that it is well-suited for absorbing sunlight and converting it into useable energy. This also indicates that $EACsSnGeI_3$ has the potential to be used in photovoltaic applications, where it can effectively capture and convert solar energy into electricity. Due to its advantageous bandgap for maximizing energy conversion efficiency, $EACsSnGeI_3$ is chosen as the perovskite active layer in the following simulation analysis.

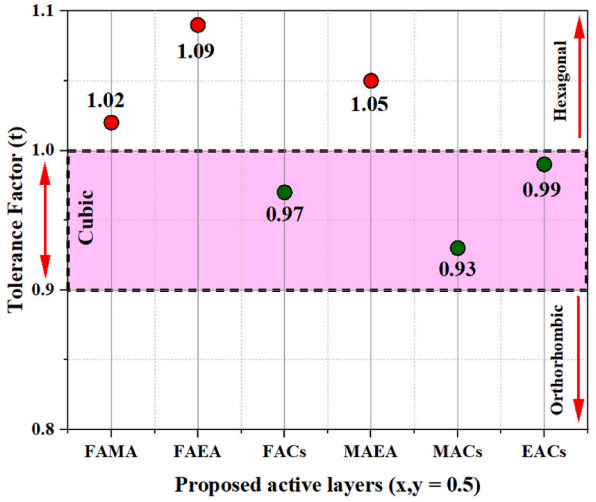

Fig. 4. Tolerance factor of mixed cation SnGe.

Table 8
Estimated bandgap of mixed cation SnGe

Single A-cation		Mixed A-cation	
Mixture	Estimate Bandgap (eV)	AA'SnGeI$_3$	Estimate Bandgap (eV)
FASnGeI$_3$	1.80	FACs	1.63
CsSnGeI$_3$	1.45		
MASnGeI$_3$	1.60	MACs	1.53
CsSnGeI$_3$	1.45		
EASnGeI$_3$	1.24	EACs	1.34
CsSnGeI$_3$	1.45		

3.3. Base modelling

The simulation configuration of the n-i-p structure (FTO/ETL/EACsSnGeI$_3$/HTL/Au) for the optimization study of solar cells is shown in Fig. 5. The initial photovoltaic (PV) characteristics of the selected perovskite material, FTO/TiO$_2$/EACsSnGeI$_3$/Spiro-OMeTAD/Au, show improved performance in terms of short-circuit current density (Jsc; 27.22 mA/cm^2), fill factor (FF; 86.84 %), and power conversion efficiency (PCE; 24.25 %) compared to CsSnGeI$_3$ (Jsc = 19.08 mA/cm^2, FF = 79.65 %, PCE = 16.99 %). However, the open circuit voltage (Voc) decreases by 8.04 % from 1.12 V to 1.03 V for CsSnGeI$_3$ and EACsSnGeI$_3$, respectively, as shown in the current-voltage (I–V) curve (Fig. 6). The decrease in Voc for EACsSnGeI$_3$ is expected due to the increase in Jsc, as both parameters scale logarithmically and as the result of the broadening of absorption spectrum (Fig. 7) with the addition of an EA and Ge into Sn-based active layer. Generally, the introduction of a mixed component with broaden and redshifted absorption spectra can potentially reduce Voc with enhance the Jsc [60]. Nevertheless, the Voc is considered to be in good agreement for perovskite solar PV (1.0–1.2 V) compared to single and multi-crystalline silicon cells (0.58–0.7 V) [61].

Table 9 tabulated the type of band offset obtained between ETL/HTL and AL. Generally, there are three type of band offset which is cliff, flat, and spike. These shapes are influenced by the valence band offset (VBO) between the HTL/AL layer and the conduction band offset (CBO) between the ETL/AL and calculated using Eq. (8) to Eq. (9) [62].

$$\mathrm{CBO} = \chi_{AL} - \chi_{ETL/HTL} \tag{8}$$

$$\mathrm{VBO} = (\chi_{AL} + Eg_{AL}) - \left(\chi_{ETL/HTL} + Eg_{ETL/HTL}\right) \tag{9}$$

Majority of proposed ETLs has cliff band offset for both conduction band and valence band expect for SnO$_2$ (flat CBO and cliff VBO). Meanwhile, Cu$_2$O has spike CBO and cliff VBO while other HTLs owned spike band. Various materials have different energy levels at different positions, poor band alignment is likely to occur at the heterojunction contact [63]. In particular, the charge transport and device performance may be impacted by the CBO and/or VBO, which is defined as the conduction/valence band difference between an absorber layer and an n-type layer due to the discontinuous band [64]. The interface band alignment is classified into three types based on the difference's energy of CBO/VBO: flat-band (CBO/VBO = 0), spike (CBO>0, VBO<0), and cliff (CBO<0, VBO<0). The flat-band offset means no band offset and consequently no barrier for the transport of generated electrons or holes (charge carrier). The spike band will prevent recombination at the interface. However, broad spike type (CBO>0.3) may block the interface carrier transport at ambient temperature. On the other hand, cliff band will increase and facilitate faster recombination at the interface [62,64]. For

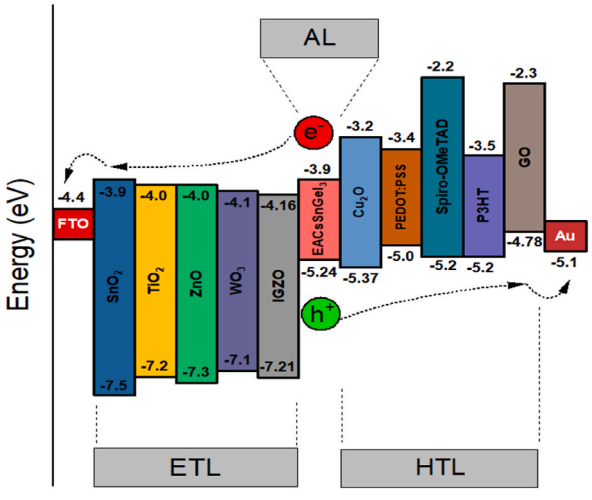

Fig. 5. Cell configuration.

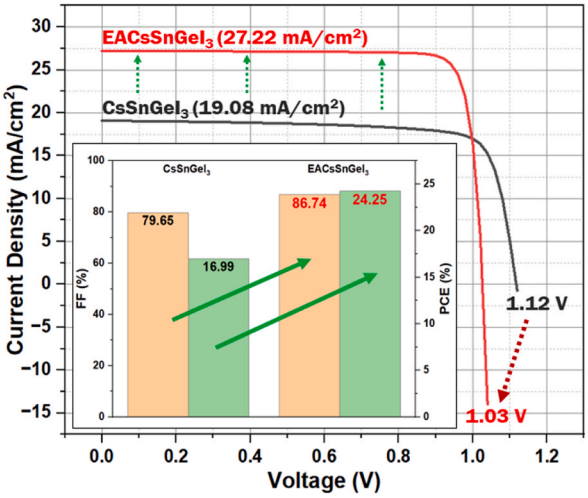

Fig. 6. I–V curve of compared materials.

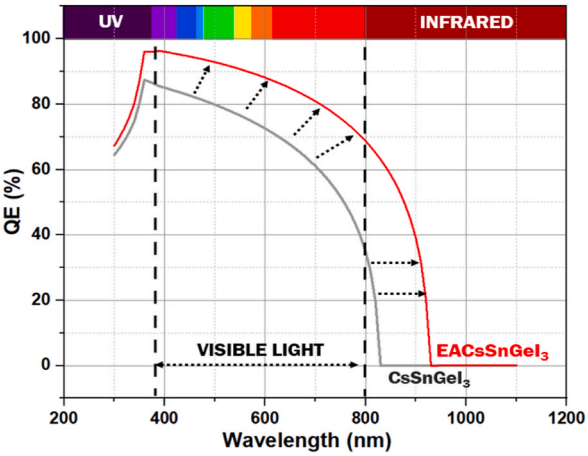

Fig. 7. QE curve of compared materials.

Table 9
Type band offset of proposed ETL/HTL and absorber

Layer	CBO (eV)	VBO (eV)	Band Type (CBO/VBO)
SnO_2	0	2.26	Flat/Cliff
TiO_2	−0.1	1.96	Cliff
ZnO	−0.1	2.06	Cliff
WO_3	−0.2	1.86	Cliff
IGZO	−0.26	1.97	Cliff
Cu_2O	0.7	0.13	Spike/Cliff
PEDOT:PSS	0.5	−0.24	Spike
Spiro-OMeTAD	1.7	−0.04	Spike
P3HT	0.4	−0.04	Spike
GO	1.6	−0.46	Spike

thin-film solar cells, a flat-band or spikes band is usually preferred as the photogenerated holes go towards the back electrode instead of the n-type layer, which means that the valence band discontinuity between an absorber layer and an n-type layer is less significant [64, 65].

The ETL and HTL are responsible for transporting electrons and holes from the perovskite layer to the electrode. They should have appropriate energy levels and good electron and hole mobility. An ETL/HTL with a higher electron affinity or lower energy level compared to the perovskite layer can help extract electrons/holes efficiently and reduce energy losses, resulting in a higher Voc [66,

67]. Additionally, the quantum efficiency (QE) of selected materials is also observed, showing a broader range of light wavelengths up to 920 nm compared to $CsSnGeI_3$ (820 nm) as shown in Fig. 7. The broadened visible light capture range in $EACsSnGeI_3$ contributes to improved power conversion efficiency (PCE), enhanced performance in different lighting conditions, and better utilization of available light [68].

3.4. Performance with different ETL and HTL

In perovskite solar cells, the Voc can be affected by various factors, including the energy levels and properties of the charge transport layers. These layers include the ETL and HTL. By carefully selecting and engineering these layers, it is possible to compensate for Voc losses and improve the overall cell performance [69]. Different ETL materials can have significant effects on the performance of these devices, such as electron injection efficiency and mobility, energy level alignment, optical properties, stability, and durability [70,71]. Instead of using typical ETL materials like TiO_2, ZnO, SnO_2, and WO_3, IGZO is used in FTO/ETL/$EACsSnGeI_3$/Spiro-OMeTAD/Au, and the photovoltaic performance is analysed as shown in Fig. 8.

The comparison of PV performance between all ETLs shows that ZnO exhibits better performance in $EACsSnGeI_3$ cells. In terms of Jsc, all ETL materials displayed nearly identical values at 27 mA/cm^2, and the Voc was closest between SnO_2, TiO_2, and ZnO, with the highest Voc recorded at 1.0425 V (SnO_2), surpassing the typical ETL (TiO_2; 1.027 V), and the lowest Voc recorded by WO_3 (0.8313 V). All ETL materials also show excellent fill factor (FF) above 80 %, with ZnO having the highest FF (88.12 %), contributing to improved power conversion efficiency (PCE; 24.84 %) compared to others. Key properties in ZnO enable effective charge extraction and minimize energy losses at the ETL interface. Additionally, ZnO has a wide bandgap of around 3.3 eV, making it transparent to visible light and having relatively high electron mobility, which facilitates efficient charge transport in the device, making it a suitable material for optoelectronic applications [72]. Furthermore, the offset of the conduction band (CB) of ZnO (−4.0 eV) with $EACsSnGeI_3$ (−3.9 eV) indicates a favourable energy level alignment for efficient electron extraction from the perovskite layer to the ZnO layer [73]. In this case, ZnO can potentially serve as a good ETL for the $EACsSnGeI_3$ layer.

The HTL in perovskite solar cells, similar to the electron transport layer, plays an important role in facilitating efficient extraction of holes, preventing recombination, and optimizing charge selectivity. The choice of HTL material and its properties can have a significant impact on the performance, efficiency, and stability of the device [71]. In this study, a cell consisting of FTO/ZnO/$EACsSnGeI_3$/HTL/Au is examined using different organic HTLs, namely Spiro-OMeTAD, PEDOT:PSS, and P3HT, as well as inorganic HTLs, such as Cu_2O and GO.

Fig. 9 shows the results of comparing different HTLs. Spiro-OMeTAD, P3HT, and Cu_2O all had a similar Jsc (approximately 27 mA/cm^2) as the ETL. On the other hand, PEDOT:PSS and GO had nearly identical Jsc of 0.9 mA/cm^2. Interestingly, P3HT had the highest FF of 88.18 % and a promising PCE of 25.19 %, surpassing Spiro-OMeTAD. P3HT is known to have a relatively high FF compared to other organic HTLs due to better carrier extraction and hole mobility. However, its PCE is lower than Cu_2O, possibly due to poor physical contact with the perovskite and a higher highest occupied molecular orbital (HOMO) energy level [74]. Additionally, PEDOT:PSS and GO showed low performance in terms of PCE, Jsc, and Voc compared to other HTLs. This suggests efficient hole transport and extraction, as both materials have a higher valence band (VB) energy level at −5.0 eV and −4.78 eV, respectively, compared to $EACsSnGeI_3$ (−5.24 eV).

By using Cu_2O as a HTL, the PCE is improved to 25.23 % compared to the typical Spiro-OMeTAD (24.84 %) and is also the highest among other materials. Cu_2O has shown promise as an HTL material in photovoltaic devices, offering advantages over perovskite. Several studies have demonstrated that Cu_2O effectively enhances the performance of PSCs. Cu_2O as an HTL exhibits high PCE due to efficient hole extraction and transport, which reduces recombination losses and improves charge collection. Additionally, the use of Cu2O as an HTL results in a longer voltage diffusion length, indicating improved charge carrier migration within the device [75–77].

Furthermore, Cu_2O has a valence band (VB) at −5.37 eV, slightly lower than EACsSnGeI3. This lower VB facilitates efficient hole extraction and transport, minimizing recombination and enhancing device performance [78]. These studies collectively provide substantial evidence for the utilization of Cu_2O as an HTL, supporting its potential to achieve high PCE, long voltage diffusion, and a favourable VB compared to perovskite. It is important to note that further research is still needed to explore the full potential of Cu_2O as an HTL material in $EACsSnGeI_3$ and to validate its applicability in various device architectures and conditions. Considering the findings from this study, Cu_2O emerges as a promising candidate for HTL applications, paving the way for advancements in PV technology, especially for narrowed bandgap perovskites.

3.5. Effects of $EACsSnGeI_3$ layer thickness

The thickness of the active layer has a significant impact on the performance, efficiency, and stability of optoelectronic devices, such as PSCs. It is crucial to optimize this parameter in order to maximize light absorption, promote charge transport, and ensure structural integrity [79]. In this study, a configuration of FTO/ZnO/$EACsSnGeI_3$ (0.3–1.5 μm)/Cu_2O/Au was used to investigate the effects of perovskite thin film thickness. The results, shown in Fig. 10 (offset 65 mA/cm^2 on y-axis) and Table 10, indicate that as the thickness of the active layer (AL) increases, the overall PV performance also increases until it reaches 1200 nm. After that, there is a slight drop in Voc, but it is not significant (<0.01 %). Meanwhile, the FF remains above 88 % until a maximum thickness of 6000 nm. Interestingly, the PCE dramatically increases to 29.48 % with just an additional 300 nm of thickness (>16 % increment) from the initial thickness. This demonstrates that the thickness of the active layer has a significant effect on the performance and efficiency of the solar cell.

The main reason for this performance is the efficient capture of light across a wide range of wavelengths, as shown in Fig. 11(a). The

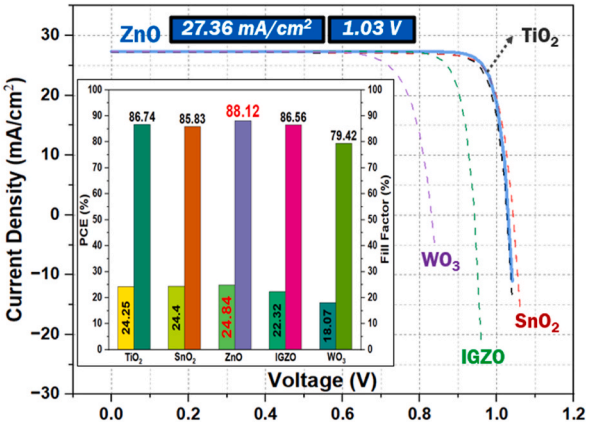

Fig. 8. I–V curves and performance of different ETLs.

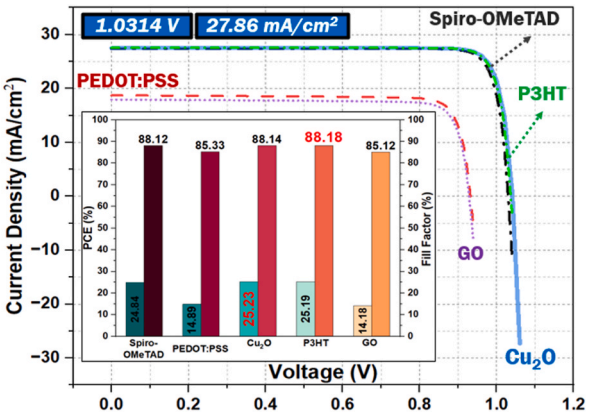

Fig. 9. I–V curves and performance of different HTLs.

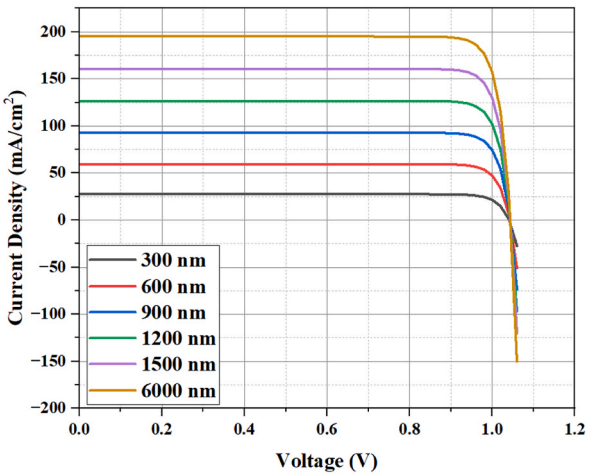

Fig. 10. I–V curve of varied active layer thickness.

Jsc and QE steadily increase up to a thickness of 6000 nm, indicating that the optimization of light absorption and charge production processes depends on the thickness of the perovskite layer. The high PCE of 31.73 % (6 μm) is achieved by increasing the thickness, which allows for more photons to be absorbed and increases the current output [80]. This study highlights the potential for PSCs with optimized thickness to achieve high efficiency levels, making them practical for real-world applications in the renewable energy sector.

Table 10
Calculated PV performance in active layer

AL thickness (nm)	Voc (V)	Jsc (mA/cm^2)	FF (%)	PCE (%)
300 (initial)	1.0410	27.4995	88.14	25.23
600	1.0446	32.0239	88.12	29.48
900	1.0453	33.2963	88.11	30.66
1200	1.0454	33.7958	88.11	31.13
1500	1.0453	34.0385	88.11	31.35
6000 (max)	1.0426	34.5235	88.11	31.73

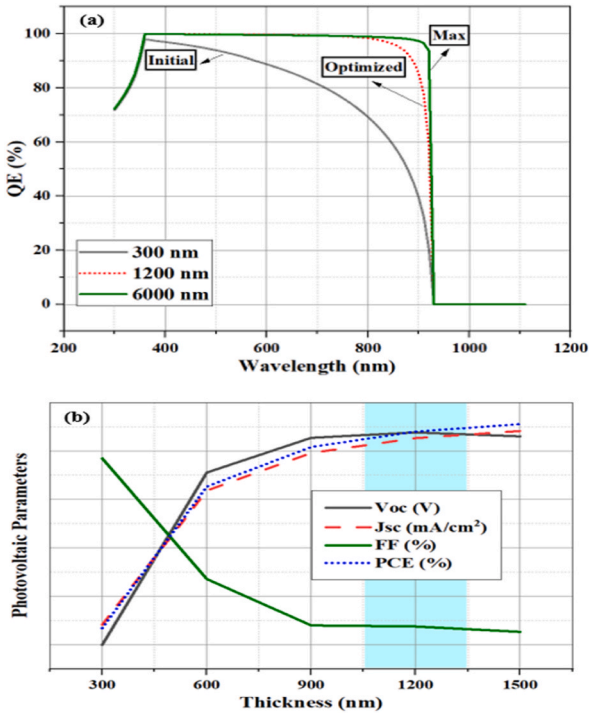

Fig. 11. (a) QE curves of initial, optimized and maximum thickness, (b) Photovoltaic performance of varied thickness.

The increase in captured light at the maximum wavelength (920 nm) from 20.36 % to 58.89 % as the perovskite layer thickness increases from 300 nm to 1200 nm indicates improved light-trapping and reduced reflection losses. A large fraction of the incident light is absorbed within the active layer, minimizing losses due to reflection or transmission [81]. The optimum thickness of 6000 nm results in an impressive absorption of 93.69 % of the incident light, maximizing the utilization of photons for efficient energy conversion.

The observed trend in quantum efficiency (QE) highlights the importance of optimizing the thickness of the perovskite layer to achieve high efficiency across a wide range of wavelengths. The thickness-dependent QE behaviour is influenced by factors such as the perovskite bandgap and absorption spectrum [82]. A maximum thickness of 6000 nm allows for effective light absorption in the visible and near-infrared spectrum, resulting in a higher QE. However, it is important to note that increasing the thickness beyond this optimized value may have negative effects on photovoltaic (PV) performance, such as higher charge recombination or deteriorated film quality.

Combined PV performance (Jsc, Voc, FF, PCE) versus active layer thickness is also shown in Fig. 11(b) to justify the selection of active layer thickness at 1200 nm. The results show that the thickness of the absorber layer has influence on PV parameters. At 0.3 μm and 0.6 μm, respectively, absorber layer thickness drops an FF from 88.14 % to 88.12 % respectively before relatively saturated beyond 0.9 μm. The measured value of Voc is 1.041 V at 0.3 μm, climbs to 1.0454 V at 1.2 μm, and then continuously to decline to 1.0426 V at 6 μm. The rise in dark saturation current is believed for the drops in Voc with thickness as a result of increase in charge carrier recombination [83]. Meanwhile, Jsc rises linearly until the absorber thickness reaches 0.9 μm, at which point it almost reaches saturation with a rising absorber thickness resulting more electron-hole pairs are created in the perovskite, which increases PCE and accounts for the significant rise in Jsc from initial absorber thickness [84]. The degree of a solar cell can extract carriers from incoming photons of a specific energy is indicated by its quantum efficiency. As also can be seen from Fig. 11(a), there is less photon absorption and photogenerated electron-hole pairs within the absorber layer at longer wavelengths, due to the decrease in absorber thickness [39]. With a 1.2 μm thick perovskite layer, the best-performing device ultimately has Jsc of 33.7958 mA/cm^2, PCE of 31.13 %, FF of

88.11 %, and Voc of 1.0454 V. Therefore, a thickness of 1.2 μm is selected for optimizing cell conditions at different operating temperatures.

3.6. Effects of different temperatures in optimized cell

The researchers evaluated the performance of perovskite solar cells (FTO/ZnO/EACsSnGeI$_3$/Cu$_2$O/Au) in different environmental conditions to determine their practical usability. They specifically studied how the optimized cells performed and remained stable at various temperatures ranging from 293 K to 313 K during realistic operation [85]. It was found that temperature has an impact on the performance of perovskite solar cells, as indicated by the data in Table 11 and Fig. 12.

The production of photocurrent in the cell remains steady as the temperature increases. This is supported by the Jsc, which is maintained at 33.7 mA/cm^2. This suggests that the EACsSnGeI$_3$ PSCs efficiently convert incoming light into electrical current due to the cell's absorption capabilities. Additionally, the Voc achieved a potential difference of more than 1 V, which is consistent with the rising temperature. This indicates that the energy levels inside the perovskite cell are well-maintained, allowing for effective charge separation and the generation of a significant voltage difference [86]. The FF also remains consistent at 87 %–88 % as the temperature increases, suggesting that the cell's ability to receive and transfer charge carriers remains unchanged. The quality of charge extraction and minimizing losses within the device are important factors that determine the overall efficiency of a solar cell [87].

The decrease in PCE from 31.49 % to 30.52 % as the temperature rises indicates a decrease in overall performance. This decrease in PCE may be due to increased carrier recombination, which occurs more frequently at higher temperatures and leads to a loss of produced photocurrent [88]. Additionally, the reduced efficiency may also be caused by changes in ionic motion and heat deterioration of the perovskite material [89]. It is worth noting that the decline in PCE in this specific cell (FTO/ZnO/EACsSnGeI$_3$/Cu$_2$O/Au) is minimal, and the cell can still achieve high efficiencies above 30 %. Absorber layer thickness and band offset between electron acceptor and donor layer has optimized the cell's PV performance. The ideal thickness of the light absorber was found to be 1.2 μm, combined with cliff band offset at ZnO/AL interface with combination of cliff/spike (CB/VB) at AL/Cu$_2$O has considerably improved the PCE, leading to a remarkable result of nearly 31 % as shown in Fig. 13.

4. Conclusion

The investigation into the effectiveness of various mixed cations in alloyed SnGe-based perovskite materials, configured with different electron transport and hole transport layers, has shown improved performance for Sn-based PSCs through compositional engineering. Additionally, the optimization of the active layer thickness and cell temperatures has also been examined. The initial evaluation of the crystal structure and optoelectronic properties indicates that EA$_{0.5}$Cs$_{0.5}$Sn$_{0.5}$Ge$_{0.5}$I$_3$ has a nearly cubic perovskite structure with a tolerance factor of 0.99 and an appropriate bandgap within the Shockley-Queisser limit for Sn-based perovskite (1.34 eV). The PV performance of Jsc, Voc, FF, PCE, and QE was further examined using the SCAPS 1-D simulator.

The solar cell, configured with FTO/ZnO/EACsSnGeI$_3$/Cu$_2$O/Au, was optimized at a temperature of 293 K with a perovskite layer thickness of 1200 nm, demonstrating remarkable stability in terms of Jsc and Voc. The cell's ability to produce photocurrent was shown to be unaffected by temperature changes, as Jsc remained unchanged at 33.7 mA/cm^2. The achieved Voc of 1 V also indicates that the energy levels inside the perovskite cell were well-maintained, allowing for effective charge separation. Additionally, the FF between 87 % and 88 %, with a PCE increase from the initial configuration of 24.25 % to an optimum condition of 31.49 % at 293 K, shows that these solar cells have successfully collected and transported charge carriers. However, experimental validation is essential to assess the accuracy of models, verify assumptions, identify discrepancies, refine parameters, and provide a robust foundation for further research and development.

CRediT authorship contribution statement

Mohd Saiful Adli Azizman: Writing – original draft, Methodology, Formal analysis. **Ayu Wazira Azhari:** Writing – review & editing, Supervision, Project administration, Funding acquisition, Conceptualization. **Naimah Ibrahim:** Writing – review & editing, Supervision, Methodology. **Dewi Suriyani Che Halin:** Resources, Conceptualization. **Suhaila Sepeai:** Validation, Methodology. **Norasikin Ahmad Ludin:** Investigation, Conceptualization. **Mohammad Nuzaihan Md Nor:** Visualization, Resources. **Ho Li Ngee:** Writing – review & editing, Resources.

Table 11
PV performance in different temperature

Parameter	293 K	298 K	303 K	308 K	313 K
Voc (V)	1.0532	1.0476	1.0421	1.0362	1.0302
Jsc (mA/cm^2)	33.7928	33.7949	33.7970	33.7991	33.8010
FF (%)	88.4852	88.1695	88.0713	87.9392	87.6391
PCE (%)	31.4930	31.2143	31.0201	30.7999	30.5189

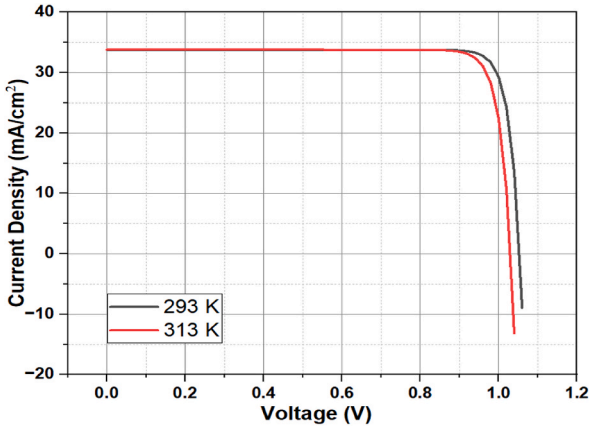

Fig. 12. I–V curves of lowest and highest studied temperature.

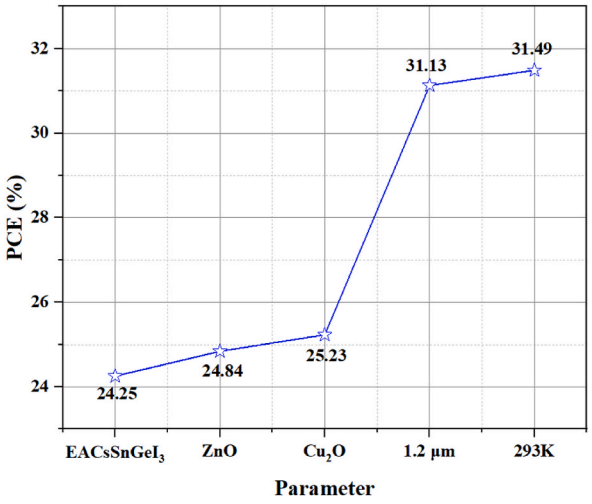

Fig. 13. Overall PV performance.

Declaration of competing interest

The authors declare the following financial interests/personal relationships which may be considered as potential competing interests Ayu Wazira Azhari reports financial support was provided by Ministry of Education Malaysia.

Acknowledgement

The authors would like to acknowledge the support from the Fundamental Research Grant Scheme under grant number FRGS/1/2021/TK0/UNIMAP/02/49 from the Ministry of Education Malaysia.

References

[1] Y. Lian, Y. Yang, L. He, X. Yang, J. Gao, C. Qin, L. Niu, X. Yang, Enhancing the luminance efficiency of formamidinium-based dion-jacobson perovskite light-emitting diodes via compositional engineering, ACS Appl. Mater. Interfaces 14 (1) (2021) 1659–1669.
[2] H.-Z. Lu, A. Krishna, S.M. Zakeeruddin, M. Grätzel, Hagfeldt Anders, Compositional and interface engineering of organic-inorganic lead halide perovskite solar cells, iScience 23 (8) (2020), 101359–101359.
[3] G.I. Choi, H.W. Choi, A study to improve the performance of mixed cation–halide perovskite-based UVC photodetectors, Nanomaterials 12 (7) (2022) 1132.
[4] N.J. Jeon, J.H. Noh, W.S. Yang, Y.C. Kim, S. Ryu, J. Seo, S.I. Seok, Compositional engineering of perovskite materials for high-performance solar cells, Nature 517 (7535) (2015) 476–480.
[5] R. Ali, Z.-G. Zhu, Q.-B. Yan, Q.-R. Zheng, G. Su, Amel Laref, Chaudry Sajed Saraj, C. Guo, Compositional engineering study of lead-free hybrid perovskites for solar cell applications, ACS Appl. Mater. Interfaces 12 (44) (2020) 49636–49647.
[6] Malekshahi Byranvand Mahdi, C. Otero-Martínez, J. Ye, W. Zuo, L. Manna, M. Saliba, , Robert, L. Polavarapu, Recent progress in mixed A-site cation halide perovskite thin-films and nanocrystals for solar cells and-light emitting diodes, Adv. Opt. Mater. 10 (14) (2022), 2200423–2200423.
[7] M. Wang, W. Wang, B. Ma, W. Shen, L. Liu, K. Cao, S. Chen, W. Huang, Lead-Free perovskite materials for solar cells, Nano-Micro Lett. 13 (1) (2021).

[8] Scopus Preview, in: Tin-based Perovskites, 2023. https://www.scopus.com/standard/marketing.uri.
[9] Q. Zhang, F. Hao, J. Li, Y. Zhou, Y. Wei, H. Lin, Perovskite solar cells: must lead be replaced – and can it be done? Sci. Technol. Adv. Mater. 19 (1) (2018) 425–442.
[10] Wafa Ayaydah, Eman Raddad, Zafer Hawash, Sn-based perovskite solar cells towards high stability and performance, 806–806 14 (4) (2023).
[11] Y.-E. Lye, K.-Y. Chan, Z.-N. Ng, A review on the progress, challenges, and performances of tin-based perovskite solar cells, Nanomaterials 13 (3) (2023), 585–585.
[12] D. Liu, Q. Li, K. Wu, Ethylammonium as an alternative cation for efficient perovskite solar cells from first-principles calculations, RSC Adv. 9 (13) (2019) 7356–7361.
[13] Z. Chu, Y. Zhao, F. Ma, C.-X. Zhang, H. Deng, F. Gao, Q. Ye, J. Meng, Z. Yin, X. Zhang, J. You, Large cation ethylammonium incorporated perovskite for efficient and spectra stable blue light-emitting diodes, Nat. Commun. 11 (1) (2020).
[14] K. Nishi, T. Oku, T. Kishimoto, N. Ueoka, A. Suzuki, Photovoltaic characteristics of CH3NH3PbI3 perovskite solar cells added with ethylammonium bromide and formamidinium iodide, Coatings 10 (4) (2020) 410.
[15] R. Chiara, M. Morana, L. Malavasi, Germanium-based halide perovskites: materials, properties, and applications, ChemPlusChem 86 (6) (2021) 879–888.
[16] I. Kopacic, B. Friesenbichler, S.F. Hoefler, B. Kunert, H. Plank, T. Rath, G. Trimmel, Enhanced performance of germanium halide perovskite solar cells through compositional engineering, ACS Appl. Energy Mater. 1 (2) (2018) 343–347.
[17] T. Krishnamoorthy, H. Ding, C. Yan, W.L. Leong, T. Baikie, Z. Zhang, M. Sherburne, S. Li, M. Asta, N. Mathews, S.G. Mhaisalkar, Lead-free germanium iodide perovskite materials for photovoltaic applications, J. Mater. Chem. A 3 (47) (2015) 23829–23832.
[18] T.K. Joshi, A. Shukla, G. Sharma, A.S. Verma, Computational determination of structural, electronic, optical, thermoelectric and thermodynamic properties of hybrid perovskite CH3CH2NH3GeI3: an emerging material for photovoltaic cell, Mater. Chem. Phys. 251 (2020) 123103.
[19] J. Seo, T. Song, S. Rasool, S. Park, J.Y. Kim, An overview of lead, tin, and mixed tin–lead-based ABI $_3$ perovskite solar cells, Advanced Energy and Sustainability Research (2023) 2200160.
[20] S. Sarker, M.T. Islam, A. Rauf, H.A. Jame, S. Ahsan, Md S. Islam, Md R. Jani, S.S. Nishat, K. Md Shorowordi, S. Ahmed, A simulation based incremental study of stable perovskite-on-perovskite tandem solar device utilizing non-toxic tin and germanium perovskite, Mater. Today Commun. 32 (2022) 103881.
[21] Y.-Q. Zhou, J. Xu, J.-B. Liu, B.-X. Liu, Alloy engineering in mixed Sn–Ge perovskites for photovoltaic application, J. Mater. Chem. A 9 (11) (2021) 6955–6961.
[22] M. Liu, H. Pasanen, H. Ali-Löytty, A. Hiltunen, K. Lahtonen, S. Qudsia, J. Smått, M. Valden, N.V. Tkachenko, P. Vivo, B-Site Co-alloying with germanium improves the efficiency and stability of all-inorganic tin-based perovskite nanocrystal solar cells, Angew. Chem. Int. Ed. 59 (49) (2020) 22117–22125.
[23] S. Pandey, A. Shukla, A. Tripathi, Elucidating the influence of native defects on electrical and optical properties in semiconducting oxides: an experimental and theoretical investigation, Comput. Mater. Sci. 210 (2022) 111037.
[24] J. Yuan, L. Zhang, C. Bi, M. Wang, J. Tian, Surface trap states passivation for high-performance inorganic perovskite solar cells, Sol. RRL 2 (10) (2018) 1800188.
[25] B. Li, B. Chang, L. Pan, L. Zihao, L. Fu, Z. He, L. Yin, Tin-based defects and passivation strategies in tin-related perovskite solar cells 5 (12) (2020) 3752–3772.
[26] R. Sa, D. Liu, Y.-T. Chen, S.-M. Ying, Mixed-cation mixed-metal halide perovskites for photovoltaic applications: a theoretical study 5 (8) (2020) 4347–4351.
[27] N. Ito, M.A. Kamarudin, D. Hirotani, Y. Zhang, Q. Shen, Y. Ogomi, S. Iikubo, T. Minemoto, K. Yoshino, S. Hayase, Mixed Sn–Ge perovskite for enhanced perovskite solar cell performance in air, J. Phys. Chem. Lett. 9 (7) (2018) 1682–1688.
[28] K. Hamada, M.A. Kamarudin, W. Zhen, D. Hirotani, Q. Shen, S. Iikubo, T. Minemoto, K. Yoshino, T. Toyoda, S. Hayase, The effect of transparent conductive oxide substrate on the efficiency of SnGe-perovskite solar cells, J. Photopolym. Sci. Technol. 32 (4) (2019) 597–602.
[29] C.H. Ng, K. Hamada, G. Kapil, M.A. Kamarudin, Z. Wang, S. Likubo, Q. Shen, K. Yoshino, T. Minemoto, S. Hayase, Reducing trap density and carrier concentration by a Ge additive for an efficient quasi 2D/3D perovskite solar cell, J. Mater. Chem. A 8 (6) (2020) 2962–2968.
[30] M.S.A. Azizman, A.W. Azhari, D.S.C. Halin, N. Ibrahim, S. Sepeai, N.A. Ludin, M.N.M. Nor, L.N. Ho, Progress in tin-germanium perovskite solar cells: a review, Synth. Met. 299 (2023) 117475.
[31] F. Sani, S. Shafie, H.N. Lim, A.O. Musa, Advancement on lead-free organic-inorganic halide perovskite solar cells: a review, Materials 11 (6) (2018) 1008.
[32] D. Ji, S. Feng, L. Wang, S. Wang, Na Mula, H. Zhang, C. Zhang, X. Li, Regulatory tolerance and octahedral factors by using vacancy in APbI3 perovskites, Vacuum 164 (2019) 186–193.
[33] Z. Zhu, Q. Sun, Z. Zhang, J. Dai, G. Xing, S. Li, X. Huang, W. Huang, Metal halide perovskites: stability and sensing-ability, J. Mater. Chem. C 6 (38) (2018) 10121–10137.
[34] Z. Zhang, Muhammad Ramlee Kamarudin, Ajay Kumar Baranwal, S. Hayase, Razey Sahamir Shahrir, Sanehira Yoshitaka, M. Chen, L. Wang, Q. Shen, S. Hayase, Sequential Passivation for Lead-Free Tin Perovskite Solar Cells with High Efficiency 61 (42) (2022).
[35] N.K. Singh, A. Agarwal, Performance assessment of sustainable highly efficient CsSn0.5Ge0.5I3/FASnI3 based Perovskite Solar Cell: a numerical modelling approach, Opt. Mater. 139 (2023) 113822.
[36] S. Yue, S.C. McGuire, H. Yan, Y.S. Chu, M. Cotlet, X. Tong, S.S. Wong, Synthesis, characterization, and stability studies of Ge-based perovskites of controllable mixed cation composition, produced with an ambient surfactant-free approach, ACS Omega 4 (19) (2019) 18219–18233.
[37] S. Abdelaziz, A. Zekry, A. Shaker, M. Abouelatta, Investigation of lead-free MASnI3-MASnIBr2 tandem solar cell: numerical simulation, Opt. Mater. 123 (2022) 111893.
[38] S. Srivastava, A.K. Singh, P. Kumar, B. Pradhan, Comparative performance analysis of lead-free perovskites solar cells by numerical simulation, J. Appl. Phys. 131 (17) (2022) 175001.
[39] H. Sabbah, Numerical simulation of 30% efficient lead-free perovskite CsSnGeI3-based solar cells, Materials 15 (9) (2022) 3229.
[40] M. Burgelman, P. Nollet, S. Degrave, Modelling polycrystalline semiconductor solar cells, Thin Solid Films 361–362 (2000) 527–532.
[41] H. MallaHasan, Ö. Onay, Investigation of the effect of different factors on the performance of several perovskite solar cells: a simulation study by SCAPS, European Journal of Engineering Science and Technology 5 (1) (2022) 20–38.
[42] M.K. Hossain, M.H.K. Rubel, G.F.I. Toki, I. Alam, Md F. Rahman, H. Bencherif, Effect of various electron and hole transport layers on the performance of $CsPbI_3$-based perovskite solar cells: a numerical investigation in dft, SCAPS-1D, and wxAMPS frameworks, ACS Omega 7 (47) (2022) 43210–43230.
[43] A. Alsalme, M.F. Altowairqi, A.A. Alhamed, R.A. Khan, Optimization of PV performance of Pb-free perovskite solar cells via numerical simulation, Molecules 28 (1) (2022) 224.
[44] N. Rai, S. Rai, P.K. Singh, P. Lohia, D.K. Dwivedi, Analysis of various ETL materials for an efficient perovskite solar cell by numerical simulation, J. Mater. Sci. Mater. Electron. 31 (19) (2020) 16269–16280.
[45] E.Shobih Widianto, E.S. Rosa, K. Triyana, N.M. Nursam, I. Santoso, Performance analysis of carbon-based perovskite solar cells by graphene oxide as hole transport layer: experimental and numerical simulation, Opt. Mater. 121 (2021) 111584.
[46] A.M. Ntouga Abena, A. Teyou Ngoupo, J.M.B. Ndjaka, Computational analysis of mixed cation mixed halide-based perovskite solar cell using SCAPS-1D software, Heliyon 8 (11) (2022) e11428.
[47] T. Minemoto, Y. Kawano, T. Nishimura, Q. Shen, K. Yoshino, S. Iikubo, S. Hayase, J. Chantana, Theoretical analysis of band alignment at back junction in Sn–Ge perovskite solar cells with inverted p-i-n structure, Sol. Energy Mater. Sol. Cell. 206 (2020) 110268.
[48] M.A. Nalianya, C. Awino, H. Barasa, V. Odari, F. Gaitho, B. Omogo, M. Mageto, Numerical study of lead free CsSn0.5Ge0.5I3 perovskite solar cell by SCAPS-1D, Optik 248 (2021) 168060.
[49] S.F. Hoefler, G. Trimmel, T. Rath, Progress on lead-free metal halide perovskites for photovoltaic applications: a review, Monatshefte Für Chemie - Chemical Monthly 148 (5) (2017) 795–826.
[50] S. Rathnayake, Hume-rothery Rules, MechCollege, 2022. https://mechcollege.com/hume-rothery-rules/.
[51] T.L. Brown, H.E. LeMay, B.E. Bursten, C. Murphy, P. Woodward, M.E. Stoltzfus, The other group 14 elements- Si, Ge, Sn, and Pb, Chemistry-The Central Science 15 (22) (2022). Pearson.
[52] F. Thaler, M. Müller, R. Spatschek, Oxygen permeation through perovskitic membranes: the influence of steam in the sweep on the permeation performance, AIMS Materials Science 3 (3) (2016) 1126–1137.

[53] A. Swarnkar, W.J. Mir, A. Nag, Can B-site doping or alloying improve thermal- and phase-stability of all-inorganic $CsPbX_3$ (X = Cl, Br, I) perovskites? ACS Energy Lett. 3 (2) (2018) 286–289.
[54] A.E. Maughan, A.M. Ganose, M.A. Almaker, D.O. Scanlon, J.R. Neilson, Tolerance factor and cooperative tilting effects in vacancy-ordered double perovskite halides, Chem. Mater. 30 (11) (2018) 3909–3919.
[55] L.E. Budd, R.M. Ibberson, W.G. Marshall, S. Parsons, The effect of temperature and pressure on the crystal structure of piperidine, Chem. Cent. J. 9 (1) (2015).
[56] K.T. Jacob, S. Raj, L. Rannesh, Vegard's law: a fundamental relation or an approximation? Int. J. Mater. Res. 98 (9) (2007) 776–779.
[57] R.A. Mackay, W. Henderson, Introduction to Modern Inorganic Chemistry, sixth ed., CRC Press, 2017.
[58] K. Wang, L. Zheng, Y. Hou, A. Nozariasbmarz, B. Poudel, J. Yoon, T. Ye, D. Yang, A.V. Pogrebnyakov, V. Gopalan, S. Priya, Overcoming Shockley-Queisser limit using halide perovskite platform? Joule 6 (4) (2022) 756–771.
[59] M. Zhu, G. Cao, Z. Zhou, Recent progress toward highly efficient tin-based perovskite (ASnX3) solar cells, Nano Select 2 (6) (2021) 1023–1054.
[60] T. Liu, R. Ma, Z. Luo, Y. Guo, G. Zhang, Y. Xiao, T. Yang, Y. Chen, G. Li, Y. Yi, X. Lu, H. Yan, B. Tang, Concurrent improvement in J_{SC} and V_{OC} in high-efficiency ternary organic solar cells enabled by a red-absorbing small-molecule acceptor with a high LUMO level, Energy Environ. Sci. 13 (7) (2020) 2115–2123.
[61] National Renewable Energy Laboratory, in: Best Research-Cell Efficiencies, 2023. https://www.nrel.gov/pv/cell-efficiency.html.
[62] H. MallaHasan, Ö. Onay, Investigation of the effect of different factors on the performance of several perovskite solar cells: a simulation study by SCAPS, European Journal of Engineering Science and Technology 5 (1) (2022) 20–38.
[63] Gansukh Mungunshagai, Z. Li, Espindola Rodriguez Moises, S. Lena, F. Martinho, López Mariño Simón, Stamate Eugen, J. Schou, O. Hansen, Canulescu Stela, Energy band alignment at the heterointerface between CdS and Ag-alloyed CZTS, Sci. Rep. 10 (1) (2020).
[64] C. Chen, X. Liu, K. Li, S. Lu, S. Wang, S. Li, Y. Lu, J. He, J. Zheng, X. Lin, J. Tang, High-efficient Sb2Se3 solar cell using Zn*x*Cd1-*x*S n-type layer, Appl. Phys. Lett. 118 (17) (2021).
[65] M. Okil, A. Shaker, M.M. Salah, T.M. Abdolkader, I.S. Ahmed, Investigation of polymer/Si thin film tandem solar cell using TCAD numerical simulation, Polymers 15 (9) (2023) 2049.
[66] C. Anrango-Camacho, K. Pavón-Ipiales, B.A. Frontana-Uribe, A. Palma-Cando, Recent advances in hole-transporting layers for organic solar cells, Nanomaterials 12 (3) (2022) 443.
[67] D.N. Qasim, Th Algwari Qais, The influence of the interface layer between the electron transport layer and absorber on the performance of perovskite solar cells, 12033–12033 1152 (1) (2021).
[68] N. Fu, Yong Bao Zhi, Y. Zhang, G. Zhang, S. Ke, P. Lin, J. Dai, H. Huang, D. Lei, Panchromatic thin perovskite solar cells with broadband plasmonic absorption enhancement and efficient light scattering management by Au@Ag core-shell nanocuboids, Nano Energy 41 (2017) 654–664.
[69] Z. Yu, L. Zhang, S. Tian, F. Zhang, B. Zhang, F. Niu, P. Zeng, J. Qu, P. Rudd, J. Huang, J. Lian, Hot-Substrate deposition of hole- and electron-transport layers for enhanced performance in perovskite solar cells, 1701659–1701659 8 (2) (2017).
[70] Marwa Dkhili, G. Lucarelli, De Rossi Francesca, B. Taheri, Khadija Hammedi, H. Ezzaouia, F. Brunetti, T.D. Brown, Attributes of high-performance electron transport layers for perovskite solar cells on flexible PET versus on glass, ACS Appl. Energy Mater. 5 (4) (2022) 4096–4107.
[71] M.K. Hossain, G.F.I. Toki, A. Kuddus, M.H.K. Rubel, M.M. Hossain, H. Bencherif, Md F. Rahman, Md R. Islam, M. Mushtaq, An extensive study on multiple ETL and HTL layers to design and simulation of high-performance lead-free CsSnCl3-based perovskite solar cells, Sci. Rep. 13 (1) (2023).
[72] C. Qiu, Y. Wu, J. Song, W. Wang, Z. Li, Efficient planar perovskite solar cells with ZnO electron transport layer, Coatings 12 (12) (2022), 1981–1981.
[73] V. Manjunath, Bimli Santosh, P.A. Shaikh, Satishchandra Ogale, R.S. Devan, Understanding the role of inorganic carrier transport layer materials and interfaces in emerging perovskite solar cells, J. Mater. Chem. C 10 (42) (2022) 15725–15780.
[74] X. Chen, B. Guo, Z. Zhang, B. Zhang, X. Zu, A. Nadege, J. Oh, Omololu Odunmbaku George, K. Chen, Y. Zhou, S. Chen, C. Yang, J. Du, K. Sun, Binary hole transport layer enables stable perovskite solar cells with PCE exceeding 24%, DeCarbon 1 (2023), 100004–100004.
[75] W. Yu, F. Li, H. Wang, Alarousu Erkki, Y. Chen, B. Lin, L. Wang, M.N. Hedhili, Y. Li, K. Wu, X. Wang, O.F. Mohammed, T. Wu, Ultrathin Cu_2O as an efficient inorganic hole transporting material for perovskite solar cells, Nanoscale 8 (11) (2016) 6173–6179.
[76] C. Lin, G. Liu, X. Xi, L. Wang, Q. Wang, Q. Sun, M. Li, Bingjie Zhu, D. Perez, Zai Huachao, The investigation of the influence of a Cu2O buffer layer on hole transport layers in MAPbI3-based perovskite solar cells, 8142–8142 15 (22) (2022).
[77] L. Lin, L. Jiang, P. Li, B. Fan, Y. Qiu, A modeled perovskite solar cell structure with a Cu2O hole-transporting layer enabling over 20% efficiency by low-cost low-temperature processing, J. Phys. Chem. Solid. 124 (2019) 205–211.
[78] M. Ismail, M. Noman, S. Tariq Jan, M. Imran, Boosting efficiency of eco-friendly perovskite solar cell through optimization of novel charge transport layers, R. Soc. Open Sci. 10 (6) (2023) 230331.
[79] N. Rai, S. Rai, P.K. Singh, P. Lohia, D.K. Dwivedi, Analysis of various ETL materials for an efficient perovskite solar cell by numerical simulation, J. Mater. Sci. Mater. Electron. 31 (19) (2020) 16269–16280.
[80] J. Xiao, L. Peng, L. Gao, J. Zhong, Z. Huang, E. Yuan, V. Srinivasapriyan, S.-F. Zhou, G. Zhan, Improving light absorption and photoelectrochemical performance of thin-film photoelectrode with a reflective substrate, RSC Adv. 11 (27) (2021) 16600–16607.
[81] B. Mulyanti, M.R. Anwar, C. Wulandari, L. Hasanah, R.E. Pawinanto, I. Hamidah, A. Rusydi, Light absorption enhancement of perovskite solar cells by a modified anti-reflection layer with corrugated void-like nanostructure using finite difference time domain methods, Phys. Scripta 98 (6) (2023) 065702.
[82] Z. Yang, Z. Yu, H. Wei, X. Xiao, Z. Ni, B. Chen, Y. Deng, S.N. Habisreutinger, X. Chen, K. Wang, J. Zhao, P.N. Rudd, J.J. Berry, M.C. Beard, J. Huang, Enhancing electron diffusion length in narrow-bandgap perovskites for efficient monolithic perovskite tandem solar cells, Nat. Commun. 10 (1) (2019).
[83] T. Ouslimane, L. Et-taya, L. Elmaimouni, A. Benami, Impact of absorber layer thickness, defect density, and operating temperature on the performance of MAPbI3 solar cells based on ZnO electron transporting material, Heliyon 7 (3) (2021) e06379.
[84] Md S. Islam, Md T. Islam, S. Sarker, H.A. Jame, S.S. Nishat, Md R. Jani, A. Rauf, S. Ahsan, K. Md Shorowordi, H. Efstathiadis, J. Carbonara, S. Ahmed, Machine learning approach to delineate the impact of material properties on solar cell device physics, ACS Omega 7 (26) (2022) 22263–22278.
[85] P. Lopez-Varo, M. Amara, S. Cacovich, A. Julien, A. Yaïche, M. Jouhari, J. Rousset, P. Schulz, J.-F. Guillemoles, J.-B. Puel, Dynamic temperature effects in perovskite solar cells and energy yield, Sustain. Energy Fuels 5 (21) (2021) 5523–5534.
[86] Z. Guo, A.K. Jena, G.M. Kim, T. Miyasaka, The high open-circuit voltage of perovskite solar cells: a review, Energy Environ. Sci. 15 (8) (2022) 3171–3222.
[87] C. Wöpke, C. Göhler, M. Saladina, X. Du, L. Nian, C. Greve, C. Zhu, K.M. Yallum, Y.J. Hofstetter, D. Becker-Koch, N. Li, T. Heumüller, I. Milekhin, D.R.T. Zahn, C. J. Brabec, N. Banerji, Y. Vaynzof, E.M. Herzig, R.C.I. MacKenzie, C. Deibel, Traps and transport resistance are the next frontiers for stable non-fullerene acceptor solar cells, Nat. Commun. 13 (1) (2022).
[88] M. Jošt, B. Lipovšek, B. Glažar, A. Al-Ashouri, K. Brecl, G. Matič, A. Magomedov, V. Getautis, M. Topič, S. Albrecht, Perovskite solar cells go outdoors: field testing and temperature effects on energy yield, Adv. Energy Mater. 10 (25) (2020) 2000454.
[89] Takeshi Tayagaki, K. Yamamoto, T.N. Murakami, Yoshita Masahiro, Temperature-dependent ion migration and mobile-ion-induced degradation of perovskite solar cells under illumination, Sol. Energy Mater. Sol. Cell. 257 (2023), 112387–112387.